analytical chemistry

pubs.acs.org/ac Article

Platinum−Nickel Nanoparticles with Enhanced Oxidase-like Activity for Total Antioxidant Capacity Bioassay

Xiaoyu Wang, Gen Wei, Wanling Liu, Yihong Zhang, Chenxin Zhu, Qi Sun, Minxuan Zhang, and Hui Wei*

Cite This: *Anal. Chem.* 2023, 95, 5937−5945 Read Online

ACCESS | Metrics & More | Article Recommendations | Supporting Information

ABSTRACT: While great progress in nanozyme-enabled analytical chemistry has been made, most current nanozyme-based biosensing platforms are based on peroxidase-like nanozymes. However, peroxidase-like nanozymes with multienzymatic activities can influence the detection sensitivity and accuracy, while the use of unstable hydrogen peroxide (H_2O_2) in a peroxidase-like catalytic reaction may result in the reproducibility challenge of sensing signals. We envision that constructing biosensing systems by using oxidase-like nanozymes can address these limitations. Herein, we reported that platinum−nickel nanoparticles (Pt−Ni NPs) with Pt-rich shells and Ni-rich cores possessed high oxidase-like catalytic efficiency, exhibiting a 2.18-fold higher maximal reaction velocity (v_{max}) than initial pure Pt NPs. The oxidase-like Pt−Ni NPs were applied to develop a colorimetric assay for the determination of total antioxidant capacity (TAC). The antioxidant levels of four bioactive small molecules, two antioxidant nanomaterials, and three cells were successfully measured. Our work not only provides new insights for preparing highly active oxidase-like nanozymes but also manifests their applications for TAC analysis.

INTRODUCTION

Nanozymes are functional nanomaterials with enzyme-like activities, which are regarded as next-generation artificial enzymes due to their distinct advantages (e.g., ease of storage, high stability, and low cost) over natural enzymes as well as conventional molecular and polymeric enzyme mimics.[1−5] Emerging from their nanoscale sizes, nanozymes possess large surface areas for bioconjugation, self-assembly abilities, and multifunctionalities.[3,6,7] By combining the enzyme-like activities with their physiochemical properties, nanozymes exhibit broad applications ranging from bioanalysis, biomedical imaging, and disease therapeutics to agriculture and environmental protection.[1,2,8−13] Among different nanozymes, enormous efforts have been devoted to developing peroxidase mimics due to their great potential for constructing bioanalytical platforms.[1,14−16] Peroxidase-like nanozymes can catalyze H_2O_2 to oxidize reducing substrates (e.g., 3,3′,5,5′-tetramethylbenzidine dihydrochloride, TMB) to generate colored products. Based on highly active peroxidase-like nanozymes, *in vitro* detection and *in vivo* bioanalysis have been performed, and various analytes, including small molecules, biomacromolecules, exosomes, and cells, were successfully detected by nanozyme-enabled detection platforms.[1,2,14,15,17−27]

Despite the remarkable progress, several challenges faced by the peroxidase-like nanozyme-based bioanalytical platforms remain to be addressed. First, H_2O_2 is destructive and easily degraded.[28] The use of unstable H_2O_2 in biosensing assays significantly compromises the high stability of peroxidase-like nanozymes, resulting in the reproducibility challenge of sensing signals. Second, peroxidase-like nanozymes generally possess multienzymatic activities (e.g., catalase- or oxidase-like activities), which may influence the detection sensitivity and accuracy. When peroxidase-like nanozymes are used for catalyzing H_2O_2 to oxidize a colorless substrate (e.g., TMB) to form a colored product, a strong background signal is generated even in the absence of H_2O_2 due to their oxidase-like activities, which greatly influences the detection sensitivity.[1,29] In addition, when nanozymes possess both peroxidase- and catalase-like activities, a decreasing colorimetric signal may be obtained because H_2O_2 is decomposed by their catalase-like activities.[1,30]

Oxidase-like nanozymes can activate molecular oxygen to oxidize reducing substrates in the absence of H_2O_2.[31,32] We envision that constructing biosensing platforms by using oxidase-like nanozymes can avoid the use of unstable H_2O_2 and provide more reliable and robust output signals. On the

Received: December 5, 2022
Accepted: March 20, 2023
Published: March 27, 2023

other hand, the catalytic activities of oxidase-like nanozymes largely determine the sensing performance of the as-developed biosensors because they measure the rate of signal generation. Therefore, the rational design of highly active oxidase-like nanozymes is needed for highly sensitive and robust detection. Several nanomaterials, such as CeO_2 nanoparticles (NPs), Pt NPs, Pd NPs, and Co_3O_4, were found to have oxidase-like activities.[1,2,31,33−36] Even so, the catalytic activities of these nanozymes were still moderate when compared with their natural counterparts. Recently, several studies confirmed that the oxidase-like activities of some nanomaterials (e.g., metal halides and MOFs) could be activated by using light as an external stimulus.[37−39] However, the use of additional light irradiation increased the complexity of the bioassays.

Among different oxidase-like nanozymes, metal NPs (e.g., Pt and Pd) with small sizes exhibited higher oxidase-like activity.[31,35,40,41] Previous studies demonstrated that doping other elements into the lattice of noble metal nanoparticles could be an effective method to enhance their catalytic activities, which may be attributed to the regulation of the metal nanoparticles' geometric and electronic structures.[41−44] Therefore, we reason that doping other transition metal elements into noble metal nanoparticles may offer an opportunity for enhancing the oxidase-like activities of metal nanoparticles. In addition, the incorporation of transition metals into noble metal nanoparticles can decrease the use of noble metals and the overall cost of metal nanoparticles.

Herein, we systematically studied the effect of doped Ni on the oxidase-like activity of Pt nanoparticles by varying the molar ratios of nickel and platinum. We demonstrated that platinum−nickel NPs (Pt−Ni NPs, molar ratio = 1:1) with Pt-rich shells and Ni-rich cores possessed the highest oxidase-like activity, which exhibited a 2.18-fold higher maximal reaction velocity (v_{max}) than initial pure Pt NPs. As a proof-of-concept demonstration, Pt−Ni NPs were employed to develop a bioanalysis platform for the total antioxidant capacity (TAC) evaluation. TAC is not only a critical indicator of the antioxidant capacity of food but can also be used for monitoring the oxidative stress level in biological systems.[45,46] Using the as-developed biosensing platform based on oxidase-like Pt−Ni NPs, the antioxidant levels of four bioactive small molecules, two antioxidant nanomaterials, and three cells were successfully measured.

EXPERIMENTAL SECTION

Chemicals and Materials. Sodium acetate (NaOAc), ascorbic acid (AA), *o*-phenylenediamine (OPD), sodium hydroxide (NaOH), benzyl alcohol, hydrochloric acid (HCl), ammonia−water ($NH_3{\cdot}H_2O$, 25−28%), and benzoic acid were purchased from Sinopharm Chemical Reagent Co., Ltd. (Shanghai, China). TMB, polyvinylpyrrolidone (PVP, M_w 80000), 2,2′-azinobis (3-ethyl benzothiazoline-6-sulfonic acid) ammonium (ABTS), hydrofluoric acid (HF), and nickel(II) acetylacetonate ($Ni(acac)_2$) were purchased from Aladdin Chemical Co., Ltd. Platinum(II) acetylacetonate ($Pt(acac)_2$), tetrapropylammonium hydroxide (TPAOH), and 5,5-dimethyl-1-pyrroline *N*-oxide (DMPO) were purchased from J&K Scientific Co., Ltd. Nb_2AlC powder was obtained from Forsman Scientific Co., Ltd. (Beijing, China). Dopamine hydrochloride and 6-hydroxy-2,5,7,8-tetramethylchromane-2-carboxylic acid (Trolox, the hydrosoluble analogue of vitamin E) were purchased from Yuanye Bio-Technology Co., Ltd. (Shanghai, China). All aqueous solutions used in the experiments were prepared with deionized water (18.2 MΩ·cm, Millipore).

Instrumentation. Transition electron microscopy (TEM) imaging was performed on a JEM-2800 (JEOL, Japan) transmission electron microscope at an acceleration voltage of 200 kV. Powder X-ray diffraction (XRD) patterns were measured by a Bruker D8 advance diffractometer at 2°/min using Cu Kα radiation. Absorption spectra were collected using a spectrophotometer (UV-3600 Plus, Shimadzu). The absorption of the 96-well plate at 652 nm was recorded by a microplate reader (Molecular Device, USA). High-angle annular dark-field scanning TEM (HAADF-STEM) and the corresponding energy-dispersive spectroscopy (EDS) elemental mappings were performed on an FEI Titan[33] G2 60-300 TEM equipped with an acceleration voltage of 300 kV and an EDS detector, respectively. Electron paramagnetic resonance (EPR) spectra were recorded on a Bruker A300 spectrometer (X-band). X-ray photoelectron spectra (XPS) were obtained by using a PHI 5000 Versa Probe XPS microscope (Ulvac-Phi, Japan). Inductively coupled plasma optical emission spectroscopy (ICP-OES) measurements were performed on an Optima 5300DV analyzer.

Synthesis of Pt−Ni NPs. The Pt−Ni nanoparticles were synthesized as follows. Briefly, 60.63 mg of $Pt(acac)_2$ (0.15 mmol), 39.60 mg of $Ni(acac)_2$ (0.15 mmol), 300 mg of benzoic acid, 80 mg of PVP, and 30 mL of benzyl alcohol were mixed by vigorous magnetic stirring. Then, the aqueous solution was sonicated for 30 min to obtain a clear solution. After sonication, the resultant solution was transferred into a Teflon-lined autoclave and heated at 180 °C for 12 h. The resulting products were precipitated by acetone and washed with an ethanol−acetone mixture six times. Finally, the obtained products were redispersed into distilled water for further use.

Pt NPs and Pt−$Ni_{0.33}$ NPs were synthesized using the same procedures described above except that the amounts of Pt and Ni precursors were different: 60.63 mg of $Pt(acac)_2$ (0.15 mmol) for Pt NPs; 60.63 mg of $Pt(acac)_2$ (0.15 mmol), and 13.20 mg of $Ni(acac)_2$ (0.05 mmol) for Pt−$Ni_{0.33}$.

To prepare Pt−Ni_2 NPs, 30.31 mg of $Pt(acac)_2$ (0.075 mmol), 39.60 mg of $Ni(acac)_2$ (0.15 mmol), 150 mg of benzoic acid, 40 mg of PVP, and 15 mL of benzyl alcohol were mixed by vigorous magnetic stirring. The other procedures were the same as the synthesis of Pt−Ni NPs.

Synthesis of Nb_2C Nanosheets (NSs). The Nb_2C NSs were obtained by HF etching and TPAOH intercalating.[47] The Nb_2AlC powder was stirred in 50% HF aqueous solution for 72 h, and the powder was washed multiple times using water with centrifugation at 11 000 rpm for 5 min until the pH was neutral. The precipitate was redispersed and stirred in 25% TPAOH aqueous solution for 36 h at room temperature. Subsequently, the precipitate was obtained by centrifuging the solution at 11 000 rpm for 5 min. Then, the precipitate was redispersed in water and sonicated for 20 min. The solution of Nb_2C nanosheets was dialyzed in water for 8 h to remove excess TPAOH. Finally, the Nb_2C NSs were obtained by collecting the supernatant after centrifuging the solution at 3500 rpm for 30 min.

Synthesis of Polydopamine NPs. Two milliliters of $NH_3{\cdot}H_2O$, 40 mL of ethanol, and 90 mL of deionized water were mixed by magnetic stirring. Then, 0.5 g of dopamine hydrochloride dissolved in 10 mL of H_2O was added into the above mixture and stirred for 24 h. Then, the resulting

https://doi.org/10.1021/acs.analchem.2c05425
Anal. Chem. 2023, 95, 5937−5945

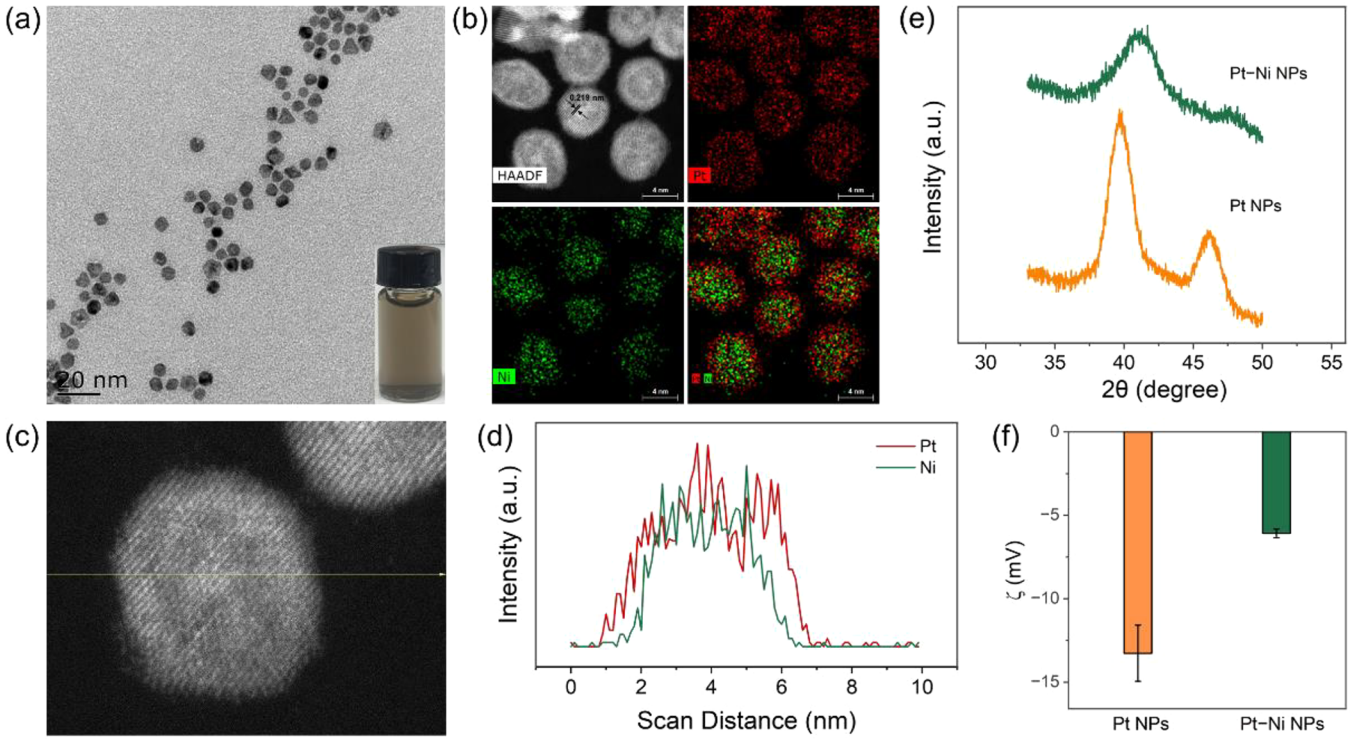

Figure 1. Characterization of Pt–Ni NPs. (a) TEM image of Pt–Ni NPs. Inset: photograph of the Pt–Ni NP aqueous suspension. (b) HAADF-STEM image and EDS elemental mapping images of Pt–Ni NPs. (c, d) EDS line scan was performed on an individual NP shown in (c) along the direction indicated by the arrow. (e) Powder X-ray diffraction patterns of Pt and Pt–Ni NPs. (f) ζ potentials of Pt and Pt–Ni NPs. Each error bar shows the standard deviation of three independent measurements.

solution was centrifuged and washed with H_2O for several times, which was then dried overnight.[48]

Oxidase-like Activity Measurements. Oxidase-like activities of the nanoparticles were evaluated by steady-state kinetics assays. Briefly, assays were conducted using TMB as a substrate at 25 °C in a 96-well plate and recorded in a microplate reader. A 0.2 M NaOAc buffer solution (pH 4.5) was used as the reaction buffer, and 5 μg/mL nanoparticles were used for their kinetics assays. Nanozymes were mixed with different concentrations of TMB in the buffer solution, and the absorbance of the reaction solution at 652 nm was immediately measured by a microplate reader. Then, the "absorbance versus time" curve was obtained, which can be used to calculate the initial reaction velocity (v). The kinetics constants (i.e., v_{max} and K_m) were obtained by fitting the reaction velocity values and the substrate concentrations to the Michaelis–Menten equation as follows:

$$v = \frac{v_{max}[S]}{K_m + [S]} \quad (1)$$

where v is the initial reaction velocity, $[S]$ is the substrate concentration, K_m is the Michaelis constant, and v_{max} is the maximal reaction velocity. The values of K_m and v_{max} can be calculated from the double reciprocal plots of eq 1.

Total Antioxidant Capacity (TAC) Determination. For TAC assays, 25 μL of Pt–Ni nanozymes (100 μg/mL) was added into 915 μL of NaOAc buffer (0.2 M, pH 4.0). Then, 50 μL of TMB (10 mM) and 10 μL of antioxidant small molecules (i.e., ascorbic acid, glutathione, cysteine, and Trolox) or antioxidant nanomaterials (i.e., Nb_2C NSs and polydopamine nanoparticles) were added. Then, the absorbance of TMBox at 652 nm was recorded using a microplate reader after incubation for 6.5 min at room temperature. The molar concentration of TMBox could be calculated by the Lambert–Beer law:

$$A = \varepsilon bc$$

where A is the absorbance at 652 nm, b is the length of light path, ε is the molar absorption coefficient ($\varepsilon_{652\ nm}$ = 39 000 M^{-1} cm^{-1}), and c is the molar concentration of TMBox.

The ΔTMBox was the relative change of TMBox in the presence and absence of antioxidant analytes in the nanozyme reaction systems. Then, the "ΔTMBox versus concentrations of analytes" curve was plotted, and the slope was defined as TAC of antioxidant analytes. Trolox-equivalent antioxidant capacity (TEAC) of antioxidant nanomaterials could be obtained by dividing their TAC with the TAC of Trolox, which represented the molar amount of Trolox with equivalent antioxidant activity per gram of nanoparticles.

Cell Culture, Lysate Preparation, and Antioxidant Level Detection. HeLa cells, human umbilical vein endothelial cells (HUVECs), and senescent HUVECs were used in this work. HeLa cells were cultured in high-glucose Dulbecco's modified Eagle's medium (DMEM), while HUVECs and senescent HUVECs were cultured in Roswell Park Memorial Institute (RPMI) 1640 medium supplemented with 10% FBS and 1% penicillin–streptomycin (10 000 U/mL) under an atmosphere of 5% CO_2 at 37 °C. A cellular aging model was constructed by simulating HUVECs with 60 μM H_2O_2 for 1 h. After 1 h, the cells were washed with PBS, and the medium was replaced with normal medium. Senescence-associated β-galactosidase staining was used to check the cellular aging model. When the cell density reached 80%, 10^8 cells were collected and washed with ice-cold

https://doi.org/10.1021/acs.analchem.2c05425
Anal. Chem. 2023, 95, 5937–5945

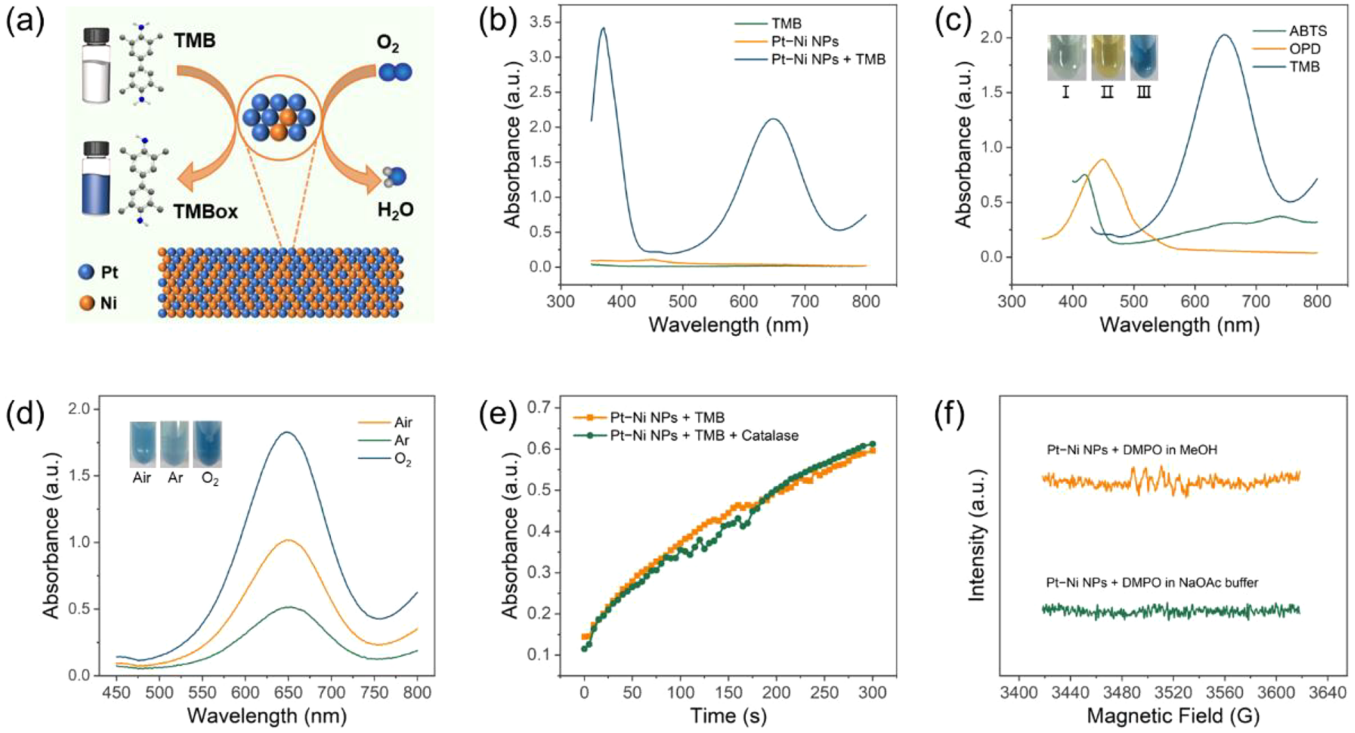

Figure 2. (a) Schematic catalytic reaction of oxidase-like activity of Pt−Ni NPs. (b) Absorption spectra of different reaction systems after catalyzing oxidation in pH 4.5, 0.2 M NaOAc buffer for 5 min. (c) Absorption spectra of 1 mM ABTS, 2 mM OPD, and 1 mM TMB after catalyzing oxidation with Pt−Ni NPs in pH 4.5 NaOAc buffer for 5 min. Inset: corresponding images showing the visual color changes of (I) ABTS, (II) OPD, and (III) TMB after the Pt−Ni NP-catalyzed reaction. (d) Absorption spectra of Pt−Ni NP-catalyzed TMB oxidation under air-, Ar-, and O_2-saturated conditions. (e) Effect of catalase on the oxidase-like activities of Pt−Ni NPs. (f) EPR spectra of Pt−Ni NPs + DMPO in NaOAc buffer and methanol solution.

phosphate-buffered saline (PBS) three times, and then the cell precipitates were suspended in 200 μL of ice-cold cell lysis buffer (containing 100 μM PMSF solution). These cells were disrupted by ultrasonication for 1 min on ice under a low power. Then, the cell lysate was centrifuged at 12 000 rpm and 4 °C for 25 min. The supernatants were transferred to sterile tubes for the following assays.

For TAC assays of three cells, 25 μL of Pt−Ni nanozymes (100 μg/mL) was added to 900 μL of NaOAc buffer (0.2 M, pH 4.0). Then, 25 μL of cell lysate (10^7/mL) and 50 μL of TMB (10 mM) were added. Then, the absorbance of TMBox at 652 nm was recorded using a microplate reader after incubation for 4.5 min at room temperature. The ΔTMBox, the relative change of TMBox in the presence and absence of cell lysate in the nanozyme reaction systems, could be calculated from the absorbance at 652 nm. Then, the antioxidant levels of cells were indicated using ΔTMBox in the presence of 2.5×10^5 cells.

RESULTS AND DISCUSSION

Synthesis and Characterization of Pt−Ni NPs. A one-step reduction strategy was developed for preparing Pt−Ni NPs. Pt(II) acetylacetonate and Ni(II) acetylacetonate with the same molar amounts were coreduced using benzyl alcohol as a solvent and reductant, benzoic acid as a nucleation inhibitor, and PVP as a coreductant and capping agent (see the Experimental Section for details). Figures 1a and S1, and S2 exhibited the typical TEM images of the Pt−Ni NPs with a diameter of about 6.2 nm. To decipher the composition of Pt−Ni NPs, ICP-OES analysis was used to determine the atomic ratio of elemental Pt to Ni (Table S1). The analyzed atomic ratio of Pt and Ni was ∼1:1, which was consistent with the ratio of precursors (i.e., Pt(II) acetylacetonate and Ni(II) acetylacetonate) added during synthesis (Table S1). To further elucidate the spatial distributions of Pt and Ni in Pt−Ni NPs, HADDF-STEM imaging coupled with EDS mapping was carried out. As shown in Figure 1b, a brighter contrast was observed in the shells of Pt−Ni NPs by the HADDF-STEM image, indicating that the structure of NPs may consist of a Ni-rich core and a Pt-rich shell. EDS mapping of Pt−Ni NPs and the line scan profile of an individual NP further confirmed that the elemental Pt and Ni were rich in the shell and core regions, respectively (Figures 1b−d and S3). Figure 1b exhibited that the distance of the adjacent fringes of Pt−Ni NPs was 0.219 nm, which was slightly smaller than face-centered cubic (fcc) Pt(111) plane with 0.225 nm due to the doped Ni atoms. In addition, XPS measurements were carried out to characterize the surface properties of Pt−Ni NPs (Figure S4). The atomic ratio of Pt and Ni detected by XPS was ∼3:1 due to the structure of Pt−Ni NPs with a Ni-rich core and a Pt-rich shell, which was consistent with the EDS mapping results (Figures 1b and S4). As shown in Figure S5, high-resolution XPS spectra demonstrated that Pt 4f and Ni 2p peaks could be clearly observed and Pt on the surface of Pt−Ni NPs was in the form of Pt(0).[43] XRD was performed to analyze the structural changes after doping Ni into Pt NPs. As shown in Figure 1e, the XRD pattern of pure Pt NPs exhibited a typical face-centered cubic (fcc) structure with the (111) diffraction peak. After forming Pt−Ni NPs, the fcc structure with the characteristic (111) diffraction peak remained. However, compared with Pt NPs, the (111) diffraction peak of Pt−Ni

https://doi.org/10.1021/acs.analchem.2c05425
Anal. Chem. 2023, 95, 5937−5945

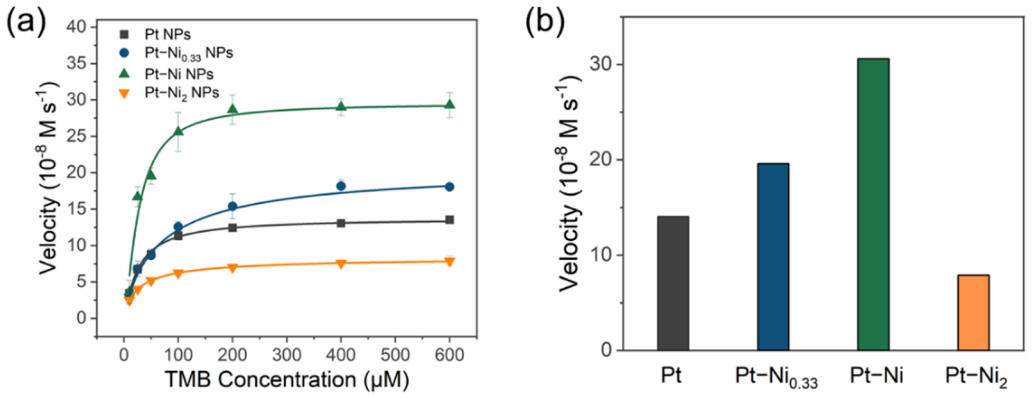

Figure 3. (a) Initial reaction velocity of different NPs as a function of TMB concentration. Each error bar shows the standard deviation of three independent measurements. (b) Histograms comparing v_{max} values of different NPs.

NPs changed to be wider and showed a clear shift toward a higher Bragg angle due to the structure of Pt-rich shells and Ni-rich cores. We also measured the ζ-potentials of Pt and Pt–Ni NPs to be −13.26 and −6.08 mV, respectively, which would facilitate their binding to a positively charged substrate (e.g., TMB) for catalysis (Figure 1f).

In addition to Pt–Ni NPs, NPs with various Pt/Ni atomic ratios were obtained by changing the molar ratios of Pt and Ni precursors (1:0, 1:0.33, and 1:2) during synthesis. ICP-OES analysis demonstrated that the atomic ratios of these as-prepared NPs were close to the molar ratios of added Pt(II) acetylacetonate and Ni(II) acetylacetonate. Pt, Pt–$Ni_{0.33}$, and Pt–Ni_2 NPs were obtained (Table S1). These as-prepared Pt, Pt–$Ni_{0.33}$, and Pt–Ni_2 with irregular spherical shapes had similar sizes with Pt–Ni NPs (Figures S6–S8).

Oxidase-like Activity Assays. After demonstrating the successful synthesis of Pt, Pt–$Ni_{0.33}$, Pt–Ni, and Pt–Ni_2 NPs, we investigated their oxidase-like activities. Among the different NPs, Pt–Ni NPs possessed the highest oxidase-like activity (vide infra). Therefore, we first took Pt–Ni NPs as an example to evaluate their oxidase-like activity by monitoring the catalytic oxidation of a typical oxidase chromogenic substrate TMB using absorption spectroscopy (Figure 2a). As shown in Figure 2b, Pt–Ni NPs along with TMB generated a deep-blue-colored oxidation product with a characteristic absorption peak centered at 652 nm, confirming the excellent oxidase-like activity of Pt–Ni NPs. In addition to TMB, two other typical oxidase substrates (i.e., ABTS and OPD) were selected to further confirm the oxidase-like activity of Pt–Ni NPs. As shown in Figure 2c, Pt–Ni NPs could also catalyze the oxidation of ABTS and OPD with dissolved oxygen in solution, producing a typical green color for oxidized ABTS and a yellow color for oxidized OPD with characteristic absorptions. Notably, under the same reaction conditions, the oxidized product of TMB (i.e., TMBox) was 51.87 μM, while only 20.86 μM ABTS was oxidized, which may be attributed to the better binding of positively charged TMB with negatively charged Pt–Ni nanozymes (Figures 1f and 2c). Moreover, the pH-dependent oxidase-like activity of Pt–Ni NPs was investigated, and they exhibited an optimal catalytic activity at about pH 4 (Figure S9).

To elucidate the catalytic mechanism, we first measured the O_2-dependent catalytic activity of Pt–Ni NPs. As shown in Figure 2d, the catalyzed oxidation of TMB enabled by Pt–Ni NPs was significantly enhanced in an O_2-saturated reaction solution and obviously inhibited in an Ar-saturated reaction solution, demonstrating that Pt–Ni NPs served as oxidase-like nanozymes rather than oxidants to catalyze the oxidation of TMB in the presence of dissolved oxygen in solution. On the other hand, oxidase can activate molecular oxygen to oxidize some reducing substrates to generate oxidized products and H_2O/hydrogen peroxide (H_2O_2)/superoxide radicals ($O_2^{\bullet-}$) by the following three possible reaction pathways:

$$\text{path 1:}\quad A_{red} + O_2 + H_2O \rightarrow A_{ox} + H_2O_2$$

$$\text{path 2:}\quad A_{red} + O_2 \rightarrow A_{ox} + H_2O$$

$$\text{path 3:}\quad A_{red} + O_2 \rightarrow A_{ox} + O_2^{\bullet-}$$

To demonstrate whether H_2O_2 was involved in the catalytic reaction, catalase, an enzyme that efficiently disproportionate H_2O_2 into O_2 and H_2O, was added to the catalytic reaction solution. As shown in Figures 2e and S10, catalase exhibited a negligible effect on the oxidase-like activity of Pt–Ni NPs, suggesting that H_2O_2 was not an intermediate during the catalytic reaction. EPR was used to detect free radicals by using 5,5-dimethyl-1-pyrroline *N*-oxide (DMPO) as the trapping agent. No obvious signals of the 1:2:2:1 4-fold signal peak and 6-fold signal peak were observed, indicating that $O_2^{\bullet-}$ and hydroxyl radicals ($^{\bullet}$OH) were not participating in the reaction process (Figure 2f). Therefore, the above results suggested that Pt–Ni NPs mediated the complete reduction of molecular oxygen to water by path 2.

A comparison of the oxidase-like activities of Pt, Pt–$Ni_{0.33}$, Pt–Ni, and Pt–Ni_2 NPs was carried out by quantifying their catalytic efficiencies using apparent steady-state kinetic assays. As shown in Figure 3a, typical Michaelis–Menten curves were obtained by plotting the initial reaction velocities as a function of TMB concentration. The kinetic parameters of Michaelis–Menten constant (K_m) and the maximum initial velocity (v_{max}) were calculated by converting the Michaelis–Menten curves into double-reciprocal plots (Figure S11). A volcano relationship could be obtained between the v_{max} values of different NPs and the Ni content, and Pt–Ni NPs exhibited the highest oxidase-like activity (Figure 3b and Table S2). In addition, a previous study demonstrated that Ni NPs exhibited negligible oxidase-like activity.[49] A comparison between the oxidase-like Pt–Ni NPs developed in this work and various reported nanozymes in the literature was performed. Obviously, Pt–Ni NPs possessed oxidase-like activity superior to that of most previously reported nanozymes (Table 1). In addition to a higher v_{max}, it was noteworthy that Pt–Ni NPs showed a much

https://doi.org/10.1021/acs.analchem.2c05425
Anal. Chem. 2023, 95, 5937−5945

Table 1. Comparison of Oxidase-like Activity of Pt−Ni NPs with Other Typical Nanozymes

nanozyme	substrate	v_{max} (μM/min)	K_m (mM)	ref
Pt−Ni NPs	TMB	18.36	0.021	this work
FeCoZn-TAC/SNC	TMB	13.38	0.459	50
Fe-N-C-400	TMB	20.28	0.269	51
Fe SAs/N_5-pC-4	TMB	6.9	0.116	52
PSMOF	TMB	8.34	0.165	38
nano-CeO_2	TMB	6	0.42	53
Mn/PSAE	TMB	4.2	0.11	54
MSN-AuNPs	TMB	7.08	0.225	55

lower K_m value, indicating a higher affinity toward TMB. The stability of Pt−Ni NPs was also studied. After storing for one year, the Pt−Ni NPs were still well dispersed and their oxidase-like activity was only slightly decreased (Figure S12).

TAC Determination of Antioxidant Small Molecules and Nanomaterials. Then, the optimized Pt−Ni NPs with oxidase-like activity were used for TAC evaluation. Figure 4a exhibited a schematic illustration of the sensing principle for TAC measurement. The oxidase-like Pt−Ni NPs could catalyze the oxidation of TMB to a blue-colored TMBox, which could be inhibited by antioxidant substances due to their competitive effects on the catalytic activity of Pt−Ni NPs. On this basis, we developed a colorimetric method for TAC assays. Four bioactive small molecules, including AA, glutathione, cysteine, and 6-hydroxy-2,5,7,8-tetramethylchromane-2-carboxylic acid (Trolox, the hydrosoluble analogue of vitamin E), were first selected as model antioxidant molecules to demonstrate the detection ability of the Pt−Ni nanozyme-based assays. The relative change of TMBox (i.e., ΔTMBox) in the presence and absence of antioxidant analytes in the nanozyme reaction systems could be calculated from the absorbance at 652 nm. ΔTMBox could be plotted as a function of antioxidant molecule concentration, and the corresponding slopes were defined as their TAC levels (Figures 4b−e and S13). As shown in Figure 4f, among the four bioactive small molecules, cysteine exhibited the highest antioxidant capacity, which was consistent with a previous report.[34]

We further demonstrated the detection ability of Pt−Ni nanozyme-based TAC assays for antioxidant nanomaterials. Two antioxidant nanomaterials, Nb_2C NSs and polydopamine NPs, were prepared according to previous literature.[47,48,56] Nb_2C NSs with antioxidant properties for effectively eliminating $^{\bullet}OH$, $O_2^{\bullet-}$, and H_2O_2 have been developed for radiation protection *in vivo*.[47] XRD, SEM, TEM, and absorption spectra demonstrated the successful synthesis of Nb_2C NSs, and their antioxidant levels were determined to be 7.76 (Figures 5a−d and S14−S16). In addition to Nb_2C NSs, polydopamine NPs were also reported for disease therapy.[48] Typically, polydopamine NPs can serve as robust antioxidants to remove excess reactive oxygen species (ROS) for alleviating the periodontal inflammation. Polydopamine NPs were prepared by a classical Stöber method, and their antioxidant levels were 0.147 (Figures 5e−g and S17). We also calculated the Trolox-equivalent antioxidant capacity (TEAC) of Nb_2C and polydopamine NPs by normalizing their TAC values using Trolox as a reference. TEAC was the molar amount of Trolox with equivalent antioxidant activity per gram of nanoparticles. Figure 5h showed that the Nb_2C NSs had a significantly higher TEAC than polydopamine NPs. These results validated that

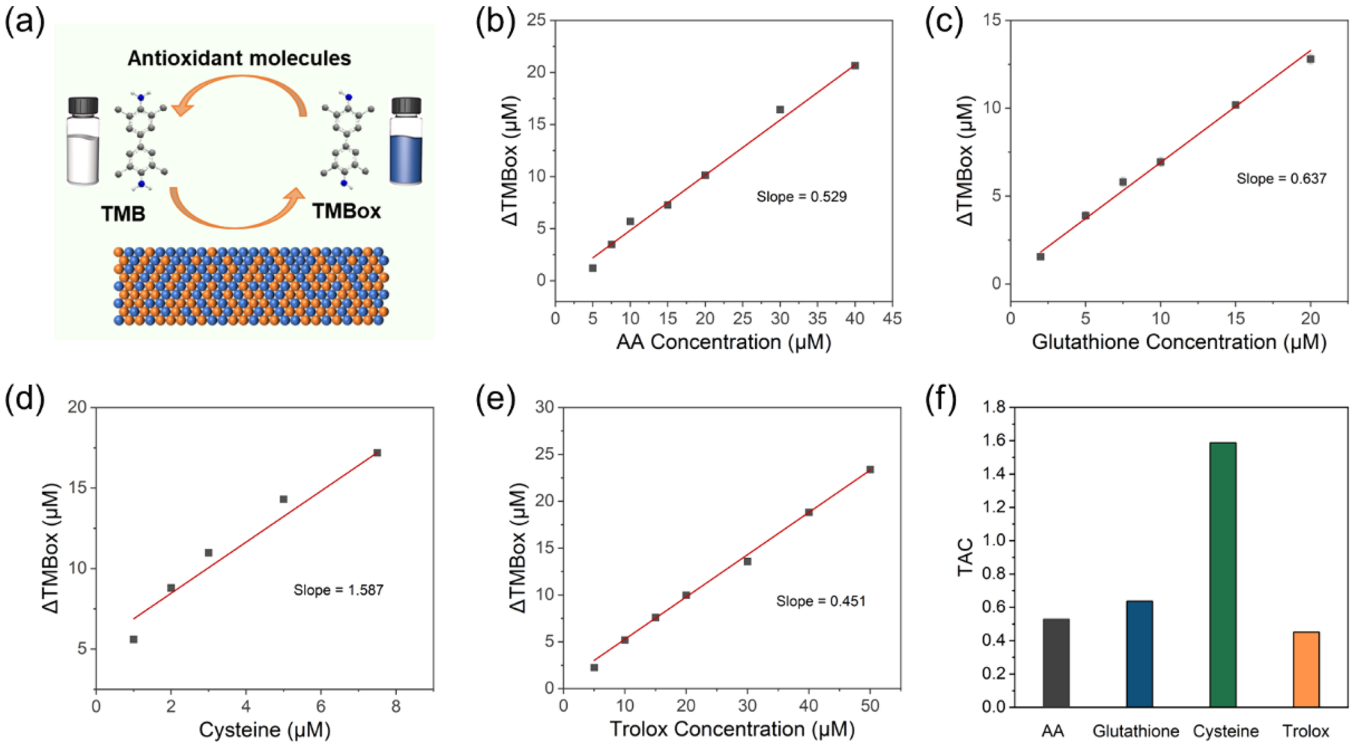

Figure 4. (a) Schematic illustration of the colorimetric assay for TAC biosensing based on Pt−Ni nanozymes. (b−e) Relative change of TMBox in the presence and absence of antioxidant small molecules in the nanozyme reaction systems (i.e., ΔTMBox) as a function of the concentrations of these molecules. Each error bar shows the standard deviation of three independent measurements. (f) Histograms comparing TAC levels of different antioxidant small molecules.

https://doi.org/10.1021/acs.analchem.2c05425
Anal. Chem. 2023, 95, 5937−5945

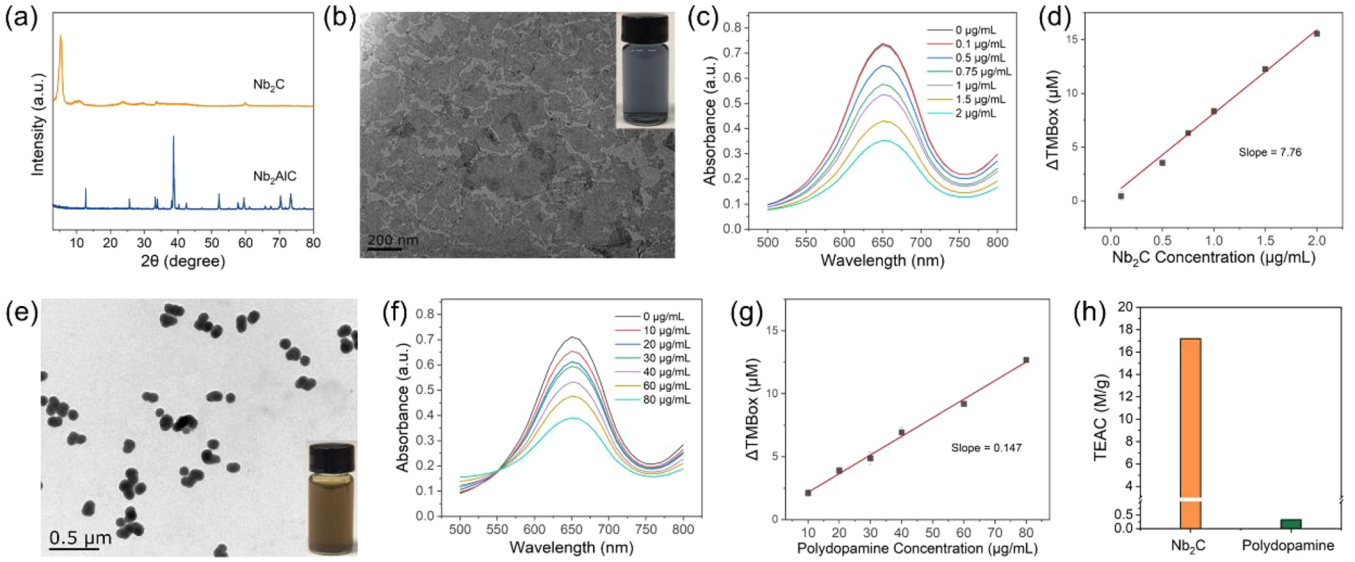

Figure 5. (a) Powder X-ray diffraction patterns of Nb_2AlC bulk and Nb_2C NSs. (b) TEM image of Nb_2C NSs. Inset: photograph of the Nb_2C NS aqueous suspension. (c) Absorption spectra for monitoring the catalytic oxidation of TMB in the presence of Pt−Ni nanozymes with various concentrations of Nb_2C NSs. (d) ΔTMBox as a function of Nb_2C NS concentrations. Each error bar shows the standard deviation of three independent measurements. (e) TEM image of polydopamine NPs. Inset: photograph of the polydopamine NP aqueous suspension. (f) Absorption spectra for monitoring the catalytic oxidation of TMB in the presence of Pt−Ni nanozymes with various concentrations of polydopamine NPs. (g) ΔTMBox as a function of polydopamine NP concentration. Each error bar shows the standard deviation of three independent measurements. (h) Histograms comparing TEAC levels of Nb_2C NSs and polydopamine NPs.

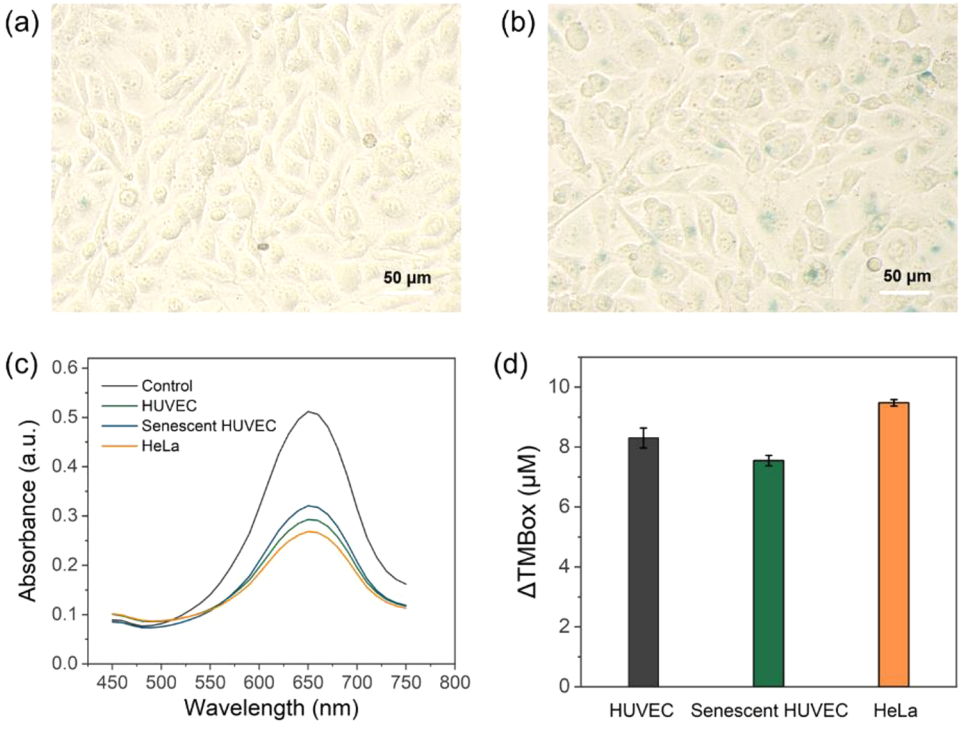

Figure 6. Senescence-associated β-galactosidase staining for (a) HUVECs and (b) HUVECs treated with 60 μM H_2O_2 for 1 h. (c) Absorption spectra for monitoring the catalytic oxidation of TMB in the presence of Pt−Ni nanozymes with various cells. (d) Histograms comparing TAC levels of different cells.

TEAC may be an indicator for the future design of antioxidant nanomaterials for the oxidative stress-induced disease therapy.

Antioxidant Level Evaluation of Cells. The Pt−Ni nanozyme-based TAC detection platform was further employed to determine the antioxidant levels in human umbilical vein endothelial cells (HUVECs), HeLa cells, and senescent HUVECs (Figures 6 and S18). A cellular aging model was successfully constructed by simulating HUVECs with H_2O_2 as determined by senescence-associated-β-galactosidase (SA-β-gal) staining (Figure 6a,b). As shown in Figure 6c,d, HeLa cells exhibited stronger antioxidant capacity than HUVECs, which could be attributed to the higher concen-

https://doi.org/10.1021/acs.analchem.2c05425
Anal. Chem. 2023, 95, 5937−5945

tration of antioxidant substances (e.g., glutathione) in tumor cells.[38,57] Moreover, when compared with normal HUVECs, the decreased antioxidant level in senescent HUVECs could be observed due to the elevated ROS level in these cells.[58]

CONCLUSIONS

In summary, we systematically studied the effect of doped Ni on the oxidase-like activity of Pt nanoparticles. Pt, Pt−$Ni_{0.33}$, Pt−Ni NPs, and Pt−Ni_2 NPs were successfully prepared by a simple one-step reduction strategy. We have demonstrated that Pt−Ni NPs consisting of Pt-rich shells and Ni-rich cores exhibited the highest oxidase-like activity. The oxidase-like Pt−Ni NPs were successfully applied to the determination of TAC and the antioxidant levels of four bioactive small molecules, two antioxidant nanomaterials, and three cells.

ASSOCIATED CONTENT

Supporting Information

The Supporting Information is available free of charge at https://pubs.acs.org/doi/10.1021/acs.analchem.2c05425.

HAADF-STEM image, EDS elemental mapping images, and XPS survey scans of Pt−Ni NPs; TEM images and kinetic curves of Pt NPs, Pt−$Ni_{0.33}$ NPs, Pt−Ni NPs, and Pt−Ni_2 NPs; absorption spectra for monitoring the catalytic oxidation of Pt−Ni nanozymes with ascorbic acid, glutathione, cysteine, and Trolox; stability of Pt−Ni NPs; SEM and TEM images of Nb_2C and polydopamine; absorption spectra of Nb_2C NSs dispersed in water; comparisons of kinetic parameters between different oxidase mimics; images for HeLa cells (PDF)

AUTHOR INFORMATION

Corresponding Author

Hui Wei − *College of Engineering and Applied Sciences, Nanjing National Laboratory of Microstructures, Jiangsu Key Laboratory of Artificial Functional Materials and State Key Laboratory of Analytical Chemistry for Life Science, School of Chemistry and Chemical Engineering, Chemistry and Biomedicine Innovation Center (ChemBIC), Nanjing University, Nanjing, Jiangsu 210023, China;* orcid.org/0000-0003-0870-7142; Phone: +86-25-89683272; Email: weihui@nju.edu.cn; Fax: +86-25-89684648; weilab.nju.edu.cn

Authors

Xiaoyu Wang − *Department of Chemistry and Material Science, College of Science, Nanjing Forestry University, Nanjing, Jiangsu 210037, China; College of Engineering and Applied Sciences, Nanjing National Laboratory of Microstructures, Jiangsu Key Laboratory of Artificial Functional Materials, Nanjing University, Nanjing, Jiangsu 210023, China;* orcid.org/0000-0002-8641-2430

Gen Wei − *College of Engineering and Applied Sciences, Nanjing National Laboratory of Microstructures, Jiangsu Key Laboratory of Artificial Functional Materials, Nanjing University, Nanjing, Jiangsu 210023, China*

Wanling Liu − *College of Engineering and Applied Sciences, Nanjing National Laboratory of Microstructures, Jiangsu Key Laboratory of Artificial Functional Materials, Nanjing University, Nanjing, Jiangsu 210023, China*

Yihong Zhang − *College of Engineering and Applied Sciences, Nanjing National Laboratory of Microstructures, Jiangsu Key Laboratory of Artificial Functional Materials, Nanjing University, Nanjing, Jiangsu 210023, China*

Chenxin Zhu − *College of Engineering and Applied Sciences, Nanjing National Laboratory of Microstructures, Jiangsu Key Laboratory of Artificial Functional Materials, Nanjing University, Nanjing, Jiangsu 210023, China*

Qi Sun − *College of Engineering and Applied Sciences, Nanjing National Laboratory of Microstructures, Jiangsu Key Laboratory of Artificial Functional Materials, Nanjing University, Nanjing, Jiangsu 210023, China*

Minxuan Zhang − *College of Engineering and Applied Sciences, Nanjing National Laboratory of Microstructures, Jiangsu Key Laboratory of Artificial Functional Materials, Nanjing University, Nanjing, Jiangsu 210023, China*

Complete contact information is available at: https://pubs.acs.org/10.1021/acs.analchem.2c05425

Author Contributions

All authors have given approval to the final version of the manuscript.

Notes

The authors declare no competing financial interest.

ACKNOWLEDGMENTS

This work was supported by the National Natural Science Foundation of China (Grants 22104055, 21874067, and 21722503), the National Key R&D Program of China (Grants 2021YFF1200700 and 2019YFA0709200), Jiangsu Provincial Key R&D Program (Grant BE2022836), the CAS Interdisciplinary Innovation Team (Grant JCTD-2020-08), the PAPD Program, the Innovation Foundation of Nanjing University, and Fundamental Research Funds for the Central Universities (Grants 202200325 and 021314380195).

REFERENCES

(1) Wu, J.; Wang, X.; Wang, Q.; Lou, Z.; Li, S.; Zhu, Y.; Qin, L.; Wei, H. *Chem. Soc. Rev.* **2019**, *48*, 1004−1076.
(2) Huang, Y.; Ren, J.; Qu, X. *Chem. Rev.* **2019**, *119*, 4357−4412.
(3) Liang, M.; Yan, X. *Acc. Chem. Res.* **2019**, *52*, 2190−2200.
(4) Wei, H.; Gao, L.; Fan, K.; Liu, J.; He, J.; Qu, X.; Dong, S.; Wang, E.; Yan, X. *Nano Today* **2021**, *40*, 101269.
(5) Zandieh, M.; Liu, J. *ACS Nano* **2021**, *15*, 15645−15655.
(6) Benedetti, T. M.; Andronescu, C.; Cheong, S.; Wilde, P.; Wordsworth, J.; Kientz, M.; Tilley, R. D.; Schuhmann, W.; Gooding, J. J. *J. Am. Chem. Soc.* **2018**, *140*, 13449−13455.
(7) Wang, Z.; Zhang, R.; Yan, X.; Fan, K. *Mater. Today* **2020**, *41*, 81−119.
(8) Kim, M. S.; Lee, J.; Kim, H. S.; Cho, A.; Shim, K. H.; Le, T. N.; An, S. S. A.; Han, J. W.; Kim, M. I.; Lee, J. *Adv. Funct. Mater.* **2020**, *30*, 1905410.
(9) Zhen, W.; Liu, Y.; Wang, W.; Zhang, M.; Hu, W.; Jia, X.; Wang, C.; Jiang, X. *Angew. Chem., Int. Ed.* **2020**, *59*, 9491−9497.
(10) Fan, K.; Cao, C.; Pan, Y.; Lu, D.; Yang, D.; Feng, J.; Song, L.; Liang, M.; Yan, X. *Nat. Nanotechnol.* **2012**, *7*, 459−464.
(11) Zhang, W.; Hu, S.; Yin, J.-J.; He, W.; Lu, W.; Ma, M.; Gu, N.; Zhang, Y. *J. Am. Chem. Soc.* **2016**, *138*, 5860−5865.
(12) Natalio, F.; Andre, R.; Hartog, A. F.; Stoll, B.; Jochum, K. P.; Wever, R.; Tremel, W. *Nat. Nanotechnol.* **2012**, *7*, 530−535.
(13) Zhao, L.; Bai, T.; Wei, H.; Gardea-Torresdey, J. L.; Keller, A.; White, J. C. *Nature Food* **2022**, *3*, 829−836.
(14) Li, S.; Zhang, Y.; Wang, Q.; Lin, A.; Wei, H. *Anal. Chem.* **2022**, *94*, 312−323.

(15) Shen, L.; Ye, D.; Zhao, H.; Zhang, J. *Anal. Chem.* **2021**, *93*, 1221−1231.
(16) Broto, M.; Kaminski, M. M.; Adrianus, C.; Kim, N.; Greensmith, R.; Dissanayake-Perera, S.; Schubert, A. J.; Tan, X.; Kim, H.; Dighe, A. S.; Collins, J. J.; Stevens, M. M. *Nat. Nanotechnol.* **2022**, *17*, 1120−1126.
(17) Loynachan, C. N.; Soleimany, A. P.; Dudani, J. S.; Lin, Y.; Najer, A.; Bekdemir, A.; Chen, Q.; Bhatia, S. N.; Stevens, M. M. *Nat. Nanotechnol.* **2019**, *14*, 883−890.
(18) Tang, Y.; Wu, Y.; Xu, W.; Jiao, L.; Chen, Y.; Sha, M.; Ye, H.-R.; Gu, W.; Zhu, C. *Anal. Chem.* **2022**, *94*, 1022−1028.
(19) Wang, L.; Li, B.; You, Z.; Wang, A.; Chen, X.; Song, G.; Yang, L.; Chen, D.; Yu, X.; Liu, J.; Chen, C. *Anal. Chem.* **2021**, *93*, 11123−11132.
(20) Wang, M.; Zhou, X.; Wang, S.; Xie, X.; Wang, Y.; Su, X. *Anal. Chem.* **2021**, *93*, 3130−3137.
(21) Ye, N.; Huang, S.; Yang, H.; Wu, T.; Tong, L.; Zhu, F.; Chen, G.; Ouyang, G. *Anal. Chem.* **2021**, *93*, 13981−13989.
(22) Zhang, C.; Chen, C.; Zhao, D.; Kang, G.; Liu, F.; Yang, F.; Lu, Y.; Sun, J. *Anal. Chem.* **2022**, *94*, 3485−3493.
(23) Zhou, X.; Fan, C.; Tian, Q.; Han, C.; Yin, Z.; Dong, Z.; Bi, S. *Anal. Chem.* **2022**, *94*, 847−855.
(24) Cai, S.; Qi, C.; Li, Y.; Han, Q.; Yang, R.; Wang, C. *J. Mater. Chem. B* **2016**, *4*, 1869−1877.
(25) Wang, C.; Ren, G.; Yuan, B.; Zhang, W.; Lu, M.; Liu, J.; Li, K.; Lin, Y. *Anal. Chem.* **2020**, *92*, 7822−7830.
(26) Wang, Q.; Wei, H.; Zhang, Z.; Wang, E.; Dong, S. *TrAC-Trend. Anal. Chem.* **2018**, *105*, 218−224.
(27) Zhang, X.; Lin, S.; Huang, R.; Gupta, A.; Fedeli, S.; Cao-Milan, R.; Luther, D. C.; Liu, Y.; Jiang, M.; Li, G.; Rondon, B.; Wei, H.; Rotello, V. M. *J. Am. Chem. Soc.* **2022**, *144*, 12893−12900.
(28) Li, H.; Li, Y.; Sun, L.; Xun, S.; Jiang, W.; Zhang, M.; Zhu, W.; Li, H. *J. Mol. Graphics Modell.* **2018**, *84*, 166−173.
(29) Huang, L.; Niu, Y.; Li, R.; Liu, H.; Wang, Y.; Xu, G.; Li, Y.; Xu, Y. *Anal. Chem.* **2019**, *91*, 5753−5761.
(30) Lin, A.; Liu, Q.; Zhang, Y.; Wang, Q.; Li, S.; Zhu, B.; Miao, L.; Du, Y.; Zhao, S.; Wei, H. *Anal. Chem.* **2022**, *94*, 10636−10642.
(31) Chong, Y.; Liu, Q.; Ge, C. *Nano Today* **2021**, *37*, 101076.
(32) Li, M.; Chen, J.; Wu, W.; Fang, Y.; Dong, S. *J. Am. Chem. Soc.* **2020**, *142*, 15569−15574.
(33) Li, Z.; Liu, F.; Jiang, Y.; Ni, P.; Zhang, C.; Wang, B.; Chen, C.; Lu, Y. *Nano Res.* **2022**, *15*, 4411−4420.
(34) Pedone, D.; Moglianetti, M.; Lettieri, M.; Marrazza, G.; Pompa, P. P. *Anal. Chem.* **2020**, *92*, 8660−8664.
(35) Lee, H.; Shin, W.; Kim, H. J.; Kim, J. *Anal. Chem.* **2021**, *93*, 16123−16132.
(36) Zhang, M.; Qu, Y.; Li, D.; Liu, X.; Niu, Y.; Xu, Y. *Anal. Chem.* **2021**, *93*, 10132−10140.
(37) Du, J.; Wang, J.; Huang, W.; Deng, Y.; He, Y. *Anal. Chem.* **2018**, *90*, 9959−9965.
(38) Liu, Y.; Zhou, M.; Cao, W.; Wang, X.; Wang, Q.; Li, S.; Wei, H. *Anal. Chem.* **2019**, *91*, 8170−8175.
(39) Liu, Y.; Wang, X.; Wei, H. *Analyst* **2020**, *145*, 4388−4397.
(40) You, J.-G.; Liu, Y.-W.; Lu, C.-Y.; Tseng, W.-L.; Yu, C.-J. *Biosens. Bioelectron.* **2017**, *92*, 442−448.
(41) Shen, X.; Liu, W.; Gao, X.; Lu, Z.; Wu, X.; Gao, X. *J. Am. Chem. Soc.* **2015**, *137*, 15882−15891.
(42) Tian, N.; Zhou, Z.-Y.; Sun, S.-G.; Ding, Y.; Wang, Z. L. *Science* **2007**, *316*, 732−735.
(43) Xi, Z.; Wei, K.; Wang, Q.; Kim, M. J.; Sun, S.; Fung, V.; Xia, X. *J. Am. Chem. Soc.* **2021**, *143*, 2660−2664.
(44) Guo, W.; Zhang, M.; Lou, Z.; Zhou, M.; Wang, P.; Wei, H. *ChemCatChem* **2019**, *11*, 737−743.
(45) Ozyurek, M.; Gungor, N.; Baki, S.; Guclu, K.; Apak, R. *Anal. Chem.* **2012**, *84*, 8052−8059.
(46) Chen, Y.; Jiao, L.; Yan, H.; Xu, W.; Wu, Y.; Wang, H.; Gu, W.; Zhu, C. *Anal. Chem.* **2020**, *92*, 13518−13524.
(47) Ren, X.; Huo, M.; Wang, M.; Lin, H.; Zhang, X.; Yin, J.; Chen, Y.; Chen, H. *ACS Nano* **2019**, *13*, 6438−6454.
(48) Bao, X.; Zhao, J.; Sun, J.; Hu, M.; Yang, X. *ACS Nano* **2018**, *12*, 8882−8892.
(49) Wang, Q.; Zhang, L.; Shang, C.; Zhang, Z.; Dong, S. *Chem. Commun.* **2016**, *52*, 5410−5413.
(50) Wu, R.; Sun, M.; Liu, X.; Qin, F.; Zhang, X.; Qian, Z.; Huang, J.; Li, Y.; Tan, T.; Chen, W.; Chen, Z. *Anal. Chem.* **2022**, *94*, 14308−14316.
(51) Xu, Y.; Xue, J.; Zhou, Q.; Zheng, Y.; Chen, X.; Liu, S.; Shen, Y.; Zhang, Y. *Angew. Chem., Int. Ed.* **2020**, *59*, 14498−14503.
(52) Chen, T.; Zhou, D.; Hou, S.; Li, Y.; Liu, Y.; Zhang, M.; Zhang, G.; Xu, H. *Anal. Chem.* **2022**, *94*, 15270−15279.
(53) Cheng, H.; Lin, S.; Muhammad, F.; Lin, Y.-W.; Wei, H. *ACS Sens.* **2016**, *1*, 1336−1343.
(54) Zhu, Y.; Wang, W.; Cheng, J.; Qu, Y.; Dai, Y.; Liu, M.; Yu, J.; Wang, C.; Wang, H.; Wang, S.; Zhao, C.; Wu, Y.; Liu, Y. *Angew. Chem., Int. Ed.* **2021**, *60*, 9480−9488.
(55) Tao, Y.; Ju, E.; Ren, J.; Qu, X. *Adv. Mater.* **2015**, *27*, 1097−1104.
(56) Zhang, C.; Wang, X.; Du, J.; Gu, Z.; Zhao, Y. *Adv. Sci.* **2021**, *8*, 2002797.
(57) Perry, R. R.; Mazetta, J.; Levin, M.; Barranco, S. C. *Cancer* **1993**, *72*, 783−787.
(58) Di Micco, R.; Krizhanovsky, V.; Baker, D.; d'Adda di Fagagna, F. *Nat. Rev. Mol. Cell Biol.* **2021**, *22*, 75−95.

https://doi.org/10.1021/acs.analchem.2c05425
Anal. Chem. 2023, 95, 5937−5945